Applied Surface Science 665 (2024) 160240

Contents lists available at ScienceDirect

Applied Surface Science

journal homepage: www.elsevier.com/locate/apsusc

Full length article

Defectivity of Al:ZnO thin films with different crystalline order probed by Positron Annihilation Spectroscopy

R. Magrin Maffei [a,b,*], M. Butterling [c], M.O. Liedke [c], S. D'Addato [a,b], A. di Bona [b], G. Bertoni [b], G.C. Gazzadi [b], S. Mariazzi [d,e], A. Wagner [c], R.S. Brusa [d,e], S. Benedetti [b]

[a] Dipartimento di Scienze Fisiche, Informatiche e Matematiche, Università di Modena e Reggio Emilia, Via Giuseppe Campi 213/a, 41125 Modena, Italy
[b] CNR-Istituto Nanoscienze, Via Giuseppe Campi 213/a, 41125 Modena, Italy
[c] Institute of Radiation Physics, Helmholtz-Zentrum Dresden-Rossendorf, Bautzner Landstr. 400, 01328 Dresden, Germany
[d] Department of Physics, University of Trento, Via Sommarive 14, 38123 Povo, Trento, Italy
[e] TIFPA/INFN Trento, Via Sommarive 14, 38123 Povo, Trento, Italy

ARTICLE INFO

Keywords:
Al-doped Zinc Oxide thin films
Crystalline order
Positron annihilation spectroscopy
Point defects
Magnetron sputtering

ABSTRACT

Three Positron Annihilation Spectroscopy (PAS) techniques have been employed to investigate the point defects of Al-doped Zinc Oxide (AZO) thin films grown by Radio Frequency (RF) magnetron sputtering with different substrates and deposition parameters. The films were grown with thickness varying from 100 to 300 nm, and their crystalline quality ranged from single crystalline epitaxial to partially amorphous. We found that the main defect in the crystalline samples is the $3V_{Zn} - V_O$ four vacancy complex, with a concentration around $10^{18} - 10^{19}$ cm^{-3}. In polycrystalline films larger vacancy clusters, within 10% – 20% of the total concentration, were detected. These vacancy clusters are inferred to be most likely located at the grain boundaries. In partially amorphous films the concentration of these larger vacancy clusters, located either at grain boundaries or in the amorphous regions of the film, approached even the 40%, and also some sub-nano voids have been observed.

1. Introduction

A special class of materials is represented by the so-called Transparent Conductive Oxides (TCOs), which are semiconductors offering an unique combination between high optical transparency and good electrical conductivity [1–5]. These properties are due to their wide band gap (> 3 eV) and to a high degree of doping, which guarantees carrier densities of the order of 10^{20}–10^{21} cm^{-3}, retaining more than 80% of transmission in the visible range.

Among these materials there is Al-doped ZnO (AZO), which is very promising because it consists of elements with far greater natural abundance than Indium Tin Oxide (ITO), which is the most employed TCO so far. AZO can be easily deposited by Radio Frequency (RF) magnetron sputtering and its properties, together with crystalline quality, can be tuned by varying substrate, dopant concentration and deposition parameters [6,7].

ZnO [8–10] and AZO [11–13] display a variety of native defects, which have a strong effect on their properties, leading to broad technological applications. Zn vacancies (V_{Zn}) are shallow acceptors [13–15] and they have been identified as the dominant compensating center in n-type ZnO by Positron Annihilation Spectroscopy (PAS) [16,17]. They can destroy the metal-like conductivity of AZO at high concentrations. The oxygen vacancy (V_O), despite being a potential donor, is a deep center [15], and then it cannot modify the electrical properties but it is optically active and absorbs light in the visible range, worsening the transparency of AZO [13]. The V_O is too small in size to be detected by positrons, but it can be detected when coupled to the V_{Zn} [18]. Other native defects, such as Zn intersitials, Zn antisites, O antisites and O interstitials, have high formation energies [14,15] and they are probably not present in large concentrations under normal conditions. Understanding which defects are present in thin AZO films and how to tailor and engineer them is then a fundamental research aspect to tune and control its electrical and optical efficiency, affecting its successful application.

PAS is a powerful tool to characterize open volume point defects, like vacancies and vacancy complexes, as well as micropores and mesopores, in bulk materials and thin films [19–22]. When positrons are implanted into a solid, they mainly lose energy in few picoseconds by ionization, electron–hole excitation and phonon scattering. After thermalization, the positrons diffuse through the lattice until they are trapped in regions of lower electron density, such as vacancies, vacancy

* Corresponding author at: Dipartimento di Scienze Fisiche, Informatiche e Matematiche, Università di Modena e Reggio Emilia, Via Giuseppe Campi 213/a, 41125 Modena, Italy.
E-mail address: riccardo.magrinmaffei@unimore.it (R. Magrin Maffei).

https://doi.org/10.1016/j.apsusc.2024.160240
Received 10 January 2024; Received in revised form 4 April 2024; Accepted 7 May 2024
Available online 10 May 2024

clusters and pores, where they subsequently annihilate with electrons. Due to their positive charge, positrons are favorably trapped in neutral or negatively charged vacancy sites. A defect profile can be obtained by employing an energy-tunable slow positron beam, in order to vary the implantation depth of the positrons.

In micropores or mesopores or at the surface of materials, positrons can form positronium (Ps), an exotic metastable atom formed by an electron and a positron. A review of the different processes of Ps formation can be found in [23]. Ps can be formed in two different spin states: the singlet state is called parapositronium (p-Ps) and decays predominantly into two γ-rays with an average lifetime of 125 ps in vacuum, while the triplet state, named orthopositronium (o-Ps), decays predominantly into three γ-rays with a mean lifetime of 142 ns in vacuum. A feature of trapped o-Ps is that it can annihilate via pick-off, a process in which the positron annihilates with another surrounding electron having opposite spin, reducing the 142 ns lifetime. In micropores the reduction reaches few nanoseconds.

The electron–positron annihilation radiation is detected and two main features are analyzed: the Doppler broadening of the 511 keV annihilation peak, in the so-called Doppler Broadening Spectroscopy (DBS), which is due mostly to the electrons momentum since positrons are thermalized, and the average positron lifetime, in the so-called Positron Annihilation Lifetime Spectroscopy (PALS). Positron lifetimes and momentum distributions differ significantly if the annihilation takes place in a defect site with respect to the perfect, defect-free lattice. In order to enhance the peak-to-background ratio and have access to the high-momentum part of the 511 keV peak, which contains annihilations with inner core electrons and carries information on the chemical surroundings of the annihilation sites, the Coincidence Doppler Broadening Spectroscopy (CDBS) technique is implemented. It is performed by detecting the annihilation radiation with two detectors and recording only simultaneous annihilation quanta. By CDBS, it is possible to increase the peak-to-background ratio roughly by three orders of magnitude, but also to improve the energy resolution by a factor $\sqrt{2}$ in comparison to that of a single detector [24–27]. The data are usually shown as ratio to a reference curve, in order to better underline the differences in the high-momentum part and/or to better identify the presence of a certain element close to the annihilation sites [25–29].

Studies of the changes in the mentioned parameters provide information on the size and quality of the positron traps, mainly through PALS; on the general amount of open volume, the diffusion length of positrons and the defect concentration, through DBS; and on the characteristics and chemical environment of the annihilation site, through CDBS. Comparison with theoretical calculations for positron lifetimes and Doppler spectra, performed via two-component Density Functional Theory (DFT), is fundamental to find the correspondence between the positron annihilation site and the type of defect.

ZnO bulk samples [16,17,30–34] and thin films [35–39] have been extensively studied with PAS, revealing the vacancy and vacancies complexes dynamics, but there are far less works about AZO [40,41] and basically there is not, to our knowledge, any detailed defect investigation about AZO thin films when thickness and crystalline order are varied, especially combining both the experimental and theoretical point of view.

In this work we studied AZO films grown by RF magnetron sputtering with different thicknesses and with different crystalline order, ranging from single crystalline epitaxial to polycrystalline and approaching the amorphous state, providing a full description of the interplay between crystalline order and defects in AZO.

2. Experimental

AZO films were deposited by RF magnetron sputtering from an undoped ZnO 3″ target (ZnO purity 99.99%) about 15 cm far from the substrate in $3 \cdot 10^{-6}$ mbar base pressure. The Argon pressure in the sputtering chamber was fixed at 5 mTorr and the deposition temperature was controlled by resistive heating and measured with a calibrated thermocouple on the sample stage. Film thickness varies between 100 and 300 nm and it has been controlled during deposition by a calibrated quartz microbalance and subsequently by means of a stylus profilometer. The Al doping was provided by DC magnetron co-sputtering from an Al target, to obtain the optimal doping concentration of ∼ 4 at.% [42]. The Al concentration was checked by Energy Dispersive X-ray Spectroscopy (EDX), performed at film surface with a FEI Quanta-200 ESEM.

Three sets of samples have been prepared. The first set has been deposited on $SrTiO_3$(110) substrates (STO) annealed in vacuum for three hours at the deposition temperature of 400 °C for degassing before growth. The deposition of AZO on this crystalline plane is driven by the good matching of the $[\bar{1}10]$ direction of STO ($\sqrt{2}a_{STO}$ = 5.5225 Å) with the $[1\bar{1}00]$ direction of ZnO ($\sqrt{3}a_{ZnO}$ = 5.6288 Å), resulting in a lattice mismatch of 1.9% [7]. The second set has been grown with the same deposition conditions on thermal SiO_2 on Si(001) substrates, obtaining polycrystalline films. The third set of samples, instead, has been prepared on UV fused quartz with thickness fixed at 100 nm and increasing Ar pressure up to 100 mTorr. Such a high pressure, combined with the ambient deposition temperature, was chosen in order to diminish the crystalline quality of the AZO films [43]. All the samples, except for the AZO/Quartz ones, have been capped with a 20 nm thick MgO layer, in order to prevent the samples from air degradation [44,45]. AZO/Quartz samples were not capped due to the need of additional surface characterization to control the film quality. The samples features are summarized in Table 1.

In order to check the crystalline quality of the samples, we resorted to X-ray Diffraction (XRD) measurements, performing $2\theta - \omega$ and ϕ scans of the AZO films with a PanAnalytical X'Pert Pro four-circle diffractometer (Cu-Kα1 wavelength, 1.5406 Å), equipped with a Göbel mirror in the incidence optics in order to obtain a parallel X-ray beam. The detection optics consisted of a 0.27° parallel plates collimator, a flat graphite monochromator and a single point gas proportional detector.

Transmission Electron Microscopy (TEM) measurements have been acquired on a Thermo Fisher Scientific Talos F200S G2 microscope at an incident energy of 200 kV on equivalent 100 nm thick AZO films grown at room temperature at 5 and 100 mTorr of Ar pressure on carbon TEM grids and on SiO_2/Si substrates. Thin cross-section lamellas of samples grown on SiO_2/Si with an area of a few microns have been obtained via Focused Ion Beam (FIB) milling after the deposition of a thin layer of metallorganic Pt at the surface to avoid damage and Ga implantation during milling. We collected diffraction patterns in TEM mode (parallel beam) on samples grown on TEM grids and Scanning TEM (STEM) images in High-Angle Annular Dark-Field (HAADF) mode on the FIB cross sections.

Variable-Energy PALS (VEPALS) measurements in the implantation energy E range 0.5−11 keV were conducted at the Mono-energetic Positron Source (MePS) beamline, which is an end station of the radiation source ELBE (Electron Linac for beams with high Brilliance and low Emittance) at Helmholtz-Zentrum Dresden-Rossendorf (HZDR) (Germany) [46]. The positron beam of MePS displays a pulse length of ∼ 250 ps (FWHM) with high repetition rate (∼ 1.625–13 MHz) and high intensity (positron flux ∼ 10^6/s). Monoenergetic positrons are implanted in materials with a profile that can be nicely approximated by the derivative of a Gaussian, the so-called Makhovian profile [47]. The implantation energy E is related to the mean positron implantation depth $\bar{z}$ by the empirical equation

$$\bar{z} = \frac{40}{\rho} E^{1.6} \tag{1}$$

where $\bar{z}$ is expressed in nm, the density of the samples ρ is given in g/cm^3 and E in keV [19]. Measuring the annihilation radiation at different implantation energies allows to characterize the defect

Table 1
Summary of the main information about the samples: substrate, thickness, growing Ar pressure and temperature, capping.

Sample number	Substrate	Thickness [nm]	Ar Pressure [mTorr]	Growing temperature [°C]	Capping
1	STO	300	5	400	20 nm MgO
2	STO	100	5	400	20 nm MgO
3	SiO_2/Si	300	5	400	20 nm MgO
4	SiO_2/Si	100	5	400	20 nm MgO
5	Quartz	100	50	Ambient	Absent
6	Quartz	100	75	Ambient	Absent
7	Quartz	100	100	Ambient	Absent

distribution at different depths. In the discussion and analysis of the depth profiling measurements one has to consider that positrons, due to their diffusion length and the implantation profile, at each implantation energy could probe from the surface to the bulk. The positron will live longer if localized into a vacancy-like defect, thanks to the depletion of the electron density. From the positron lifetime, then, size and defect type can be extracted and even secondary defects may be resolved into the spectrum. A PALS spectrum can be fitted as the convolution of a resolution function $R(t)$, often modeled with a set of Gaussians, with a sum of exponential functions expressed as

$$F(t) = R(t) \circledast \sum_i \frac{I_i}{\tau_i} e^{-\frac{t}{\tau_i}} + BKG \quad (2)$$

where τ_i and I_i are the lifetimes and their associated intensities and BKG is the background. The intensities must sum to one. From the intensities of the lifetimes components the defect concentrations can be extracted, given that not all the positrons annihilate in defects (saturation) [48].

The annihilation γ-rays are recorded by using a lifetime $CeBr_3$ scintillator detector with a homemade software employing a Teledyne SPDevices ADQ14DC-2X digitizer for fast analog-to-digital conversion with 14-bit vertical resolution, 2GS/s (GigaSamples per second) horizontal resolution and pulse detection performed on an integrated FPGA. The timing reference is derived from the precision master oscillator of the superconducting LINAC and it is phase-matched to the electron bunches of the beam with a temporal jitter of 14 ps (FWHM). The signal-to-noise ratio is above 10^4 with a lifetime resolution of around 230 ± 10 ps (FWHM) [46,49]. The resolution function required for spectrum analysis uses two Gaussian functions with distinct intensities depending on the positron implantation energy E and appropriate relative shifts. All spectra contained at least 10^7 counts. The spectra were deconvoluted into discrete lifetime components using the non-linearly least-squared-based package PALSfit fitting software [50]. The lifetime spectra fits have been considered good with a reduced chi-squared of less than 1.1.

DBS measurements were carried out using a continuous monoenergetic positron beam having a maximum positron implantation energy E of 35 keV [51]. The annihilation γ-ray energy spectrum is collected by a High-Purity Ge (HPGe) detector system with an energy resolution of 1.09 keV (FWHM) at the 511 keV γ-line. The Doppler broadening of the γ-ray spectrum is monitored by the S parameter and W parameter defined respectively as the counts of the central window (511.00 ± 0.93 keV) and the wing windows (508.33 ± 0.49 keV and 513.67 ± 0.49 keV) to the counts of the total annihilation peak. Depending on the annihilation site, the positrons "see" electrons with different momenta: a positron trapped into a vacancy or a vacancy complex will annihilate more probably with valence electrons, since cores are farther away, determining an increase of the S parameter with respect to the defect-free lattice. Changes in the defectivity will be hence reflected in the S and W parameters, which can be normalized to a reference sample to gain information about the main defect and to compare data from different apparatuses [52]. To find the characteristic S and W parameters of the films, the $S(E)$ and $W(E)$ were fitted with the standard model based on the solution of the positron stationary diffusion-annihilation equation [53,54], by employing the software VEPFIT [55]. At each positron implantation energy, the S parameter (and so W) can be expressed as a linear combination of the characteristic S values of the positron annihilation in the surface, the bulk, and the different defect-states, respectively

$$S(E) = f_s(E)S_s + f_b(E)S_b + \sum_i f_{di}(E)S_{di} \quad (3)$$

where $f_s(E)$, $f_b(E)$ and $f_{di}(E)$ are the fractions of positrons annihilating at the surface (or in the MgO capping layer), in the bulk and in defect-states, respectively. From the positron diffusion length the total defect concentration can be evaluated via the standard trapping model [53,54], even in case of saturation trapping [48]. Together with the AZO films, we also measured an hydrothermally (HT) grown ZnO bulk single crystal (SurfaceNet GmbH) as a reference to normalize the Doppler data, which is a standard procedure to compare data obtained in different laboratories [52]. These measurements are shown in Fig. 1 of the Supporting Information (SI).

DFT calculations of the positron lifetimes and Doppler curves have been performed with the ATSUP code [56–60], which evaluates the positron wave function for a superposition of atoms for a given atomic structure, in the Boronski–Nieminen (BN) scheme, which is usually in a better agreement with experiment than lifetimes calculated using the Gradient-Correction (GC) approach [56–59]. In many systems, the generation of defects causes an inward or outward relaxation of the neighboring atoms. We could not calculate the relaxed structure, which has to be given to the code before. Hence, these results have to be taken as an approximation, but this is the approach of the majority of calculations about positron lifetimes in ZnO in literature [34,61–63], because of the difficulty in modeling lattice relaxations on defects, especially at a high degree of disorder.

3. Results and discussion

3.1. Crystalline structure

ZnO films are well known to grow preferentially c-axis oriented [42,64], showing only the ZnO(0002) peak (at 34.42° [65]) in the X-ray diffraction spectrum, and our films make no exception, as shown in Fig. 1**a** for the AZO/Quartz film grown at 5 mTorr. However, while the in-plane grain orientation is expected to be totally random in AZO/SiO_2/Si films, which are indeed polycrystalline, we demonstrated that AZO/STO films are epitaxial [7], as it can be understood from the ϕ scan of the ZnO(0002) peak presented in Fig. 1**b**, where it can be seen the six-fold symmetry of the ZnO(0001) plane.

From XRD measurements we previously estimated [7] the vertical (along the normal to the substrate surface) and lateral (parallel to it) Coherence Length (CL) of epitaxial AZO/STO films and polycrystalline AZO/SiO_2/Si films. The CL is defined as the average extension of the crystal lattice which scatter coherently, thus devoid of macroscopical defects like grain boundaries, and it is a measure of the grain size. ZnO displays a columnar growth and then the vertical and lateral CLs can differ significantly. The data are in Table 2: epitaxial and thicker films have bigger CLs, meaning their crystalline quality is better.

When the films are deposited on quartz at high Ar pressure, a drastic decrease of the ZnO(0002) peak can be observed (Fig. 1**a**) when the Ar pressure in the sputtering chamber was increased, together with the appearance of other two very low intensity peaks, which are attributed

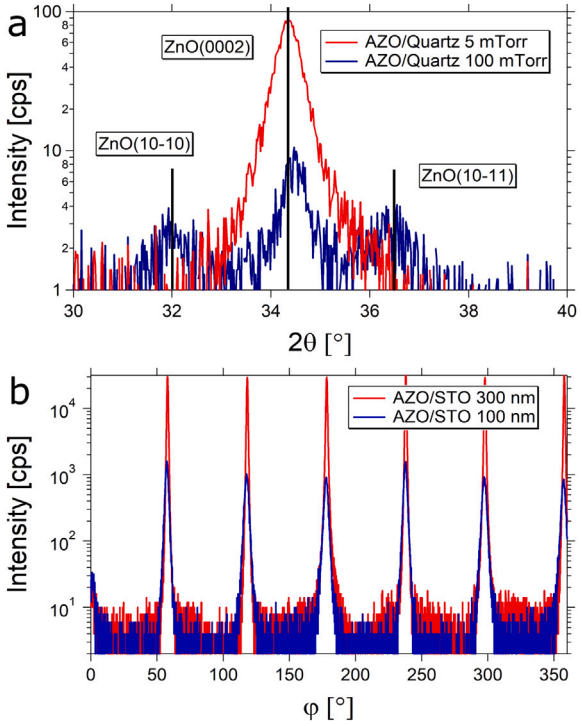

Fig. 1. XRD measurements: **(a)** $2\theta - \omega$ scans of the AZO/Quartz films deposited at 5 and 100 mTorr and **(b)** ϕ scans of the ZnO(0002) peak of the AZO/STO films.

Table 2
Vertical and lateral coherence length of AZO/STO and AZO/SiO_2/Si films from Magrin Maffei et al. [7].

Sample	Vertical CL [nm]	Lateral CL [nm]
AZO/STO 300 nm	140 ± 15	42 ± 2
AZO/STO 100 nm	98 ± 11	48 ± 2
AZO/SiO_2/Si 300 nm	75 ± 4	20 ± 1
AZO/SiO_2/Si 100 nm	36 ± 2	10 ± 1

to the ZnO(10$\bar{1}$0) and ZnO(10$\bar{1}$1) reflection at 31.77° and 36.25°, respectively. The area under the three peaks of the sample grown at 100 mTorr is lower by a factor of about 10 than the area under the single ZnO(0002) peak of the sample grown at 5 mTorr, so the overall crystalline quality is decreased, with smaller grains, as well as more orientations with respect to the substrate plane are introduced.

To determine the degree of disorder, TEM characterization has been performed to compare 100 nm thick samples grown at 5 and 100 mTorr. To quantitatively compare their crystalline quality, two electron diffraction patterns from the AZO films grown on TEM grids in plan-view have been acquired at the very same conditions of condenser illumination and objective focus. The profiles have been plotted after azimuthal integration in Fig. 2. To avoid effects of preferential orientation (evident in the polycrystalline sample), the whole diffraction profile intensities have been integrated after background subtraction to account for the tail of the central transmitted spot (best fit). As a result, the sample grown at 100 mTorr loses the 33% of the diffracted intensity with respect to the one grown at 5 mTorr, which is due to an increased amorphous part in the film.

STEM images of the thin FIB cross-sectional milled samples have been taken in HAADF mode (inner cutoff angle > 50 mrad) as shown in Fig. 3, where the AZO films are comprised between the black substrate (SiO_2) at the bottom and the Pt protective layer at the top. The film grown at 5 mTorr is very homogeneous and does not show any feature. The film grown at 100 mTorr, instead, is characterized by many black spots, which in HAADF indicate the presence of areas where electrons

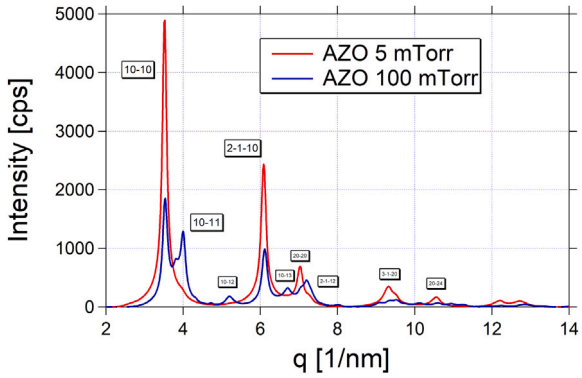

Fig. 2. Azimuthal average of the TEM diffraction patterns of AZO films deposited at 5 and 100 mTorr.

are less scattered in the sample. These black spots, then, are probably voids or pores in the film.

3.2. Positron Annihilation Lifetime Spectroscopy

Variable positron implantation energy allowed us to probe the samples from the very surface to the entire thickness of the films and also to the substrate. The positron lifetime spectra were fitted using the PALSfit program with three or four lifetime components. SiO_2/Si and quartz substrate display a long lifetime component of around 1.4–1.5 ns, which drastically increase the average positron lifetime. The same happens at the surface due to annihilation of positrons in surface traps and/or formation of positronium. Hence, implantation energies associated to the AZO films are easily recognizable in the depth profiling from the region where the average positron lifetime is at minimum. In AZO/STO films the substrate shows instead a lower positron average lifetime due to the STO single crystal, but since the films have the same thicknesses of AZO/SiO_2/Si films, the implantation energies associated to the films are the same. Following this procedure, we can individuate the lifetimes associated to the films looking at measurements approximately in the range 2–7.5 keV for 300 nm thick films and 2–4.5 keV for the 100 nm thick films.

The VEPALS depth profiles of AZO/STO films are shown in Fig. 4. The MgO capping layer shows a characteristic lifetime of 370 ps, which has been fixed in all the analysis. In the AZO films, a single lifetime τ_1 of 250–265 ps with more than 95% intensity is observed. Notice that the lifetime of defect-free bulk ZnO of 150–160 ps [30,32,33,66,67] is not observed. This means we are in saturation trapping regime: the almost totality of the positrons get trapped and annihilate in defects.

The VEPALS depth profiles of AZO/SiO_2/Si films are shown in Fig. 5. In the films, most of the positrons are still getting trapped into a defect with lifetime τ_1 in the range 250–265 ps, but with an intensity slightly lower, around the 80–90%. A second lifetime τ_2 arises in the films, going from ~ 370–400 ps in the 300 nm thick film to ~ 400–420 ps in the 100 nm thick film, revealing an increase in the size of vacancy complexes. The increasing fraction of positrons annihilating into larger and larger vacancy complexes is consistent with the decrease of crystalline quality and grain size in polycrystalline films with respect to epitaxial ones and when the AZO films thickness is decreased, as reported in Table 2. The component τ_3, shown only in intensity in Fig. 5, is a characteristic lifetime of the SiO_2 substrate, due to o-Ps formation and pick-off annihilation in its voids.

This trend is even more pronounced when examinating AZO/Quartz films grown at increasing Ar pressure, whose VEPALS depth profiles are shown in Fig. 6. Here there is no capping, but only the surface dynamics of AZO films at low implantation energy. In the film grown at 50 mTorr, the behavior is similar to the 100 nm thick AZO/SiO_2/Si film of Fig. 5**b**,**d**, with the most intense component τ_1 still in the

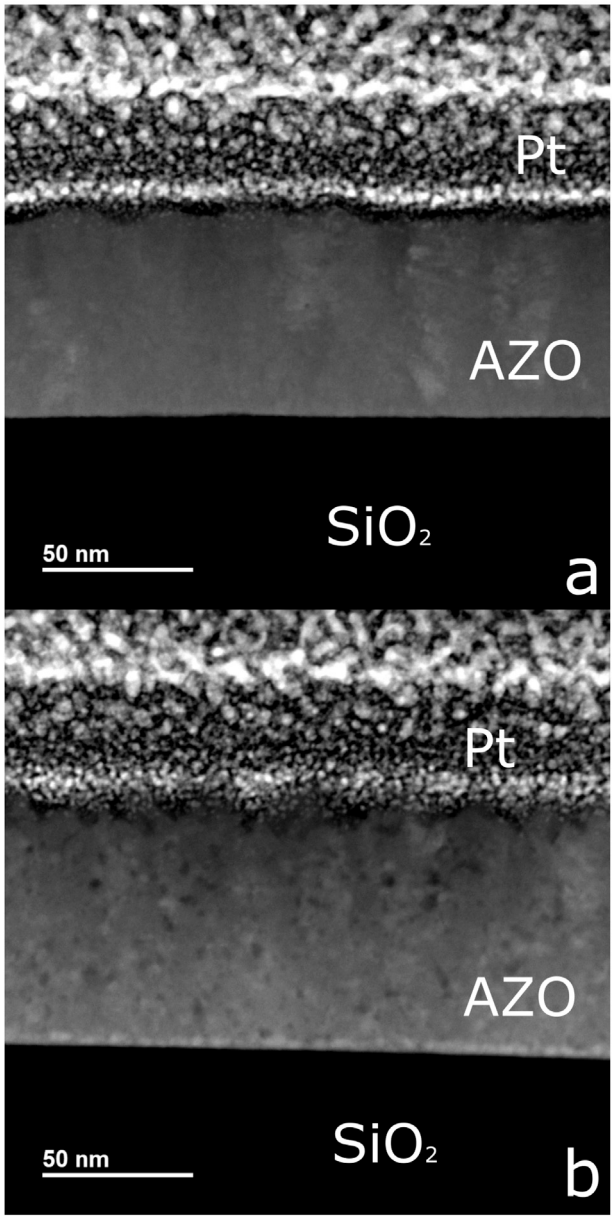

Fig. 3. **(a)** STEM HAADF cross sectional image of the AZO film grown at 5 mTorr and **(b)** STEM HAADF cross sectional image of the AZO film grown at 100 mTorr.

range 250–265 ps with an intensity around the 80% and a second component of around 400–500 ps. The film grown at 75 mTorr, shown in Fig. 2 of the SI, has a similar behavior. Instead, in the film grown at 100 mTorr, the intensity of the second component τ_2 increases approaching almost 40%, while the first component becomes slightly shorter, around 230–240 ps. This means that positrons are also trapped into larger vacancy complexes. These complexes can be located both in the amorphous part and at boundaries of the grains that are becoming smaller and smaller with the increase of the Ar deposition pressure. This is in good agreement with the structural characterization reported in Section 3.1 and the decrease in the diffusion length of positrons (see Section 3.4). In particular, the decrease in the positron diffusion length indicates that the grain sizes decrease and they are efficiently trapped by defects at grain boundaries. Nevertheless, the majority of positrons still annihilate at small complexes, slightly smaller, which could be located either in the bulk of a grain or at the grain boundaries. In addition, a longer component τ_3 of around 1.5%–2% of intensity is present in films deposited at more than 50 mTorr and an even longer component τ_4 of more than 7 ns of about 1% of intensity is present in films deposited at 75 and 100 mTorr. These components were not shown in Fig. 6 due to their low intensities, but they substantially enhance by a lot the weighted average positron lifetime τ_{av}, shown in Fig. 7**a**. These long lifetimes are arguably associated to o-Ps pick-off annihilations in sub-nano voids, compatible to the previous TEM investigation. Therefore, the total average positron lifetime τ_{av}, which is a measure of the total open volume defectivity of the samples, shows a dramatic increase for film deposited at high Ar pressure, whilst it is more or less constant to values close to τ_1 for the other films. Fig. 7**b** shows the average intensities of the first two components of the lifetime spectra in the films, where it can be seen that the second component is absent in AZO/STO films, appears in AZO/SiO_2 films and increases further in AZO/Quartz films with increasing Ar pressure.

3.3. ATSUP calculations

ATSUP calculations have been exploited to determine how the lifetime changes with vacancy size. Spherical vacancy clusters around a reference atom were generated by sequentially removing the next-nearest atoms, up to a total of 12 missing atoms. The results of our calculations are shown in Fig. 8, together with calculations from Chen et al. [62], for comparison. The calculated bulk lifetime of around 154 ps is in good agreement with the literature [30,32,33,66,67] and also our results for lifetimes in defects are in good agreement with the literature [30,34,61–63]. Chen et al. in their calculation with ATSUP find longer lifetimes for large vacancy cluster defects, maybe because the Semiconductor Model (SM) [68] instead of the BN scheme has been used there for the short-range enhancement of the electron density.

Results for small vacancy clusters, up to four vacancies, are shown in Table 3, together with references from the literature. As it can be seen, the majority of the previous calculations employed the ATSUP method in BN scheme, without lattice relaxation, as in the present work. Nevertheless, here the full defect landscape is calculated and a very large supercell of 864 atoms is employed, while for instance Chen et al. use a supercell of only 128 atoms. Only Brauer et al. and Procházka et al. included relaxation but only for simple vacancies and the V_{Zn}–V_O divacancy, where the authors associated a defect with a lifetime of 260 ps to the V_{Zn}–V_O divacancy [30]. From comparison with the calculated lifetimes, reported in Table 3, we can attribute the shorter component τ_1 of ~ 250–265 ps, observed in all the samples except for the AZO/Quartz film grown at 100 mTorr, to a small vacancy complex, most probably a four vacancy cluster which could be either a $V_{Zn}-3V_O$, a $3V_{Zn} - V_O$ or a $2(V_{Zn} - V_O)$. It will be shown later, in Section 3.5, that thanks to CDBS measurements a more precise assignment to this small vacancy complex can be given. In the AZO/Quartz film grown at 100 mTorr, τ_1 is around 230–240 ps and comparison with theory seems to indicate smaller defects like the $V_{Zn} - 2V_O$ or $2V_{Zn} - V_O$. The calculated lifetimes of the $3V_{Zn} - V_O$ and $V_{Zn} - 2V_O$ vacancy complexes are shown as a dashed lines in Figs. 4–6 as references. Similar small vacancy complexes, like the $V_{Zn} - nV_O$ with $n = 1$–3, have already been observed in ZnO thin films grown by Pulsed Laser Deposition (PLD) [38] and RF magnetron sputtering [41,69]. This τ_1 could be associated to the $V_{Zn} - V_O$ divacancy like Brauer did, but, as it will be explained later, CDBS measurements point towards a leading defect of at least four vacancies.

The second lifetime τ_2, observed in AZO/SiO_2/Si and AZO/Quartz films, is always above 370 ps and our calculations never reach such a long lifetime, while the ones from Chen et al. approach a lifetime of about 375 ps for complexes of 12 vacancies. Hence these defects are arguably greater than 12 vacancies [34,41,61,62]. This larger vacancy complexes are most likely localized at grain boundaries [70], as it was already revealed by PAS [71–73].

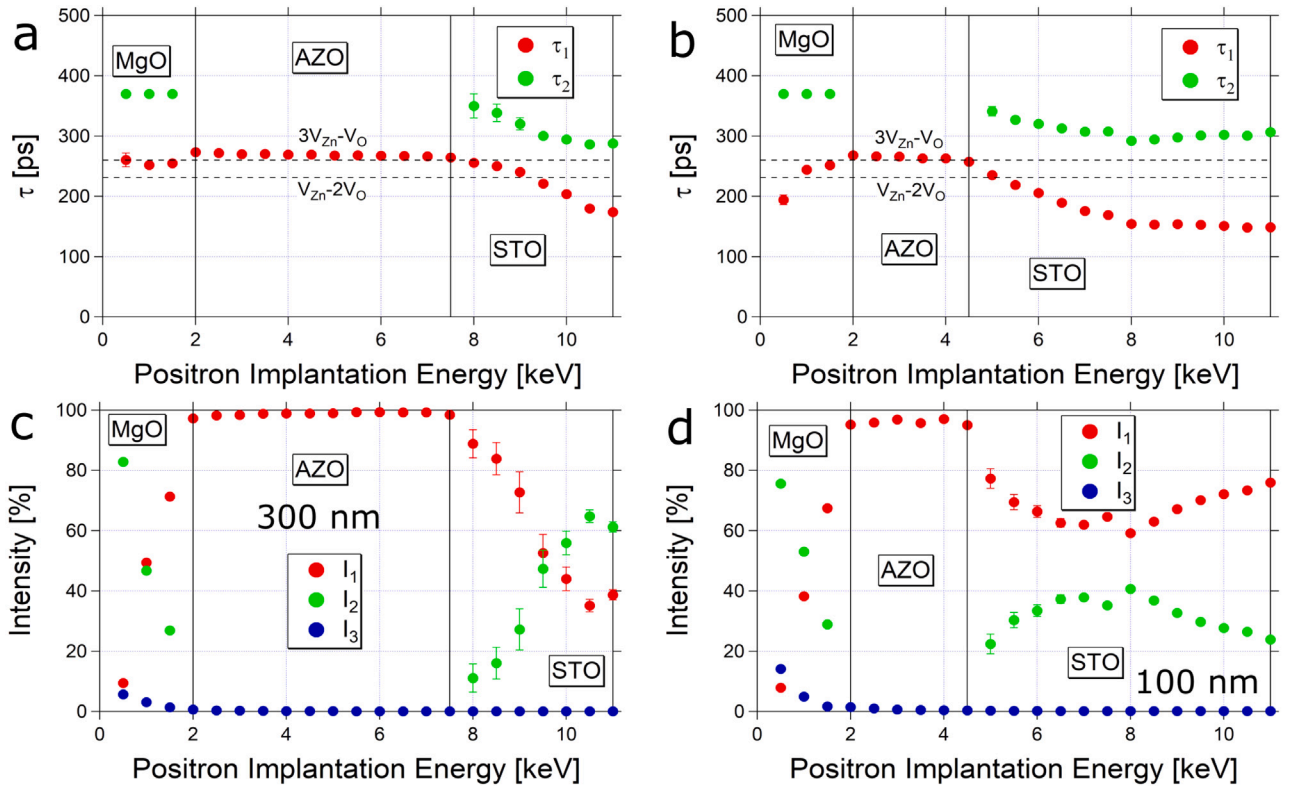

Fig. 4. VEPALS depth profiles for the AZO/STO films. **(a)** Lifetimes in the 300 nm film, **(b)** lifetimes in the 100 nm film, **(c)** intensities in the 300 nm film and **(d)** intensities in the 100 nm film. Dotted lines mark the calculated lifetimes associated to the $3V_{Zn} - V_O$ and $V_{Zn} - 2V_O$ vacancy clusters. Regions assigned to the layers are marked. The error bars are within the dots size if not visible.

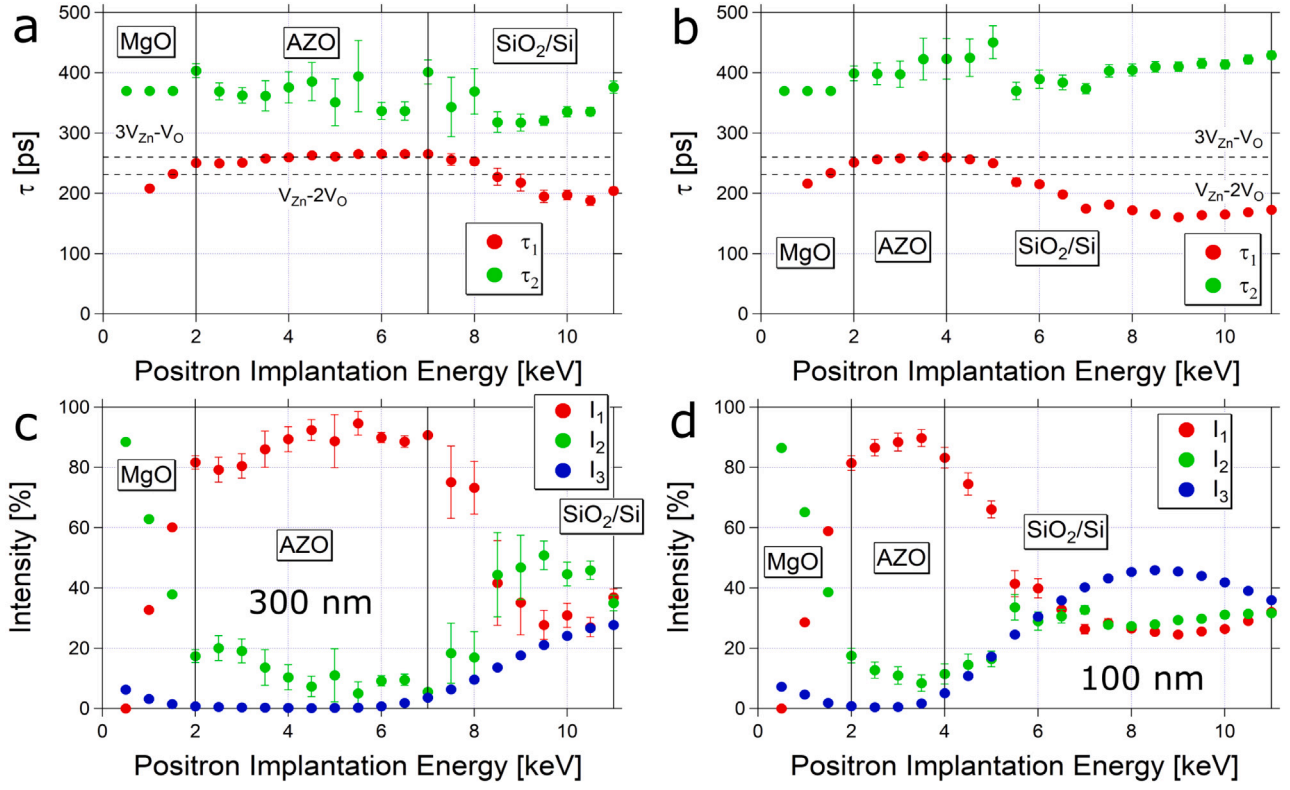

Fig. 5. VEPALS depth profiles for the AZO/SiO_2/Si films. **(a)** Lifetimes in the 300 nm film, **(b)** lifetimes in the 100 nm film, **(c)** intensities in the 300 nm film and **(d)** intensities in the 100 nm film. Dotted lines mark the calculated lifetimes associated to the $3V_{Zn} - V_O$ and $V_{Zn} - 2V_O$ vacancy clusters. Regions assigned to the layers are marked. The error bars are within the dots size if not visible.

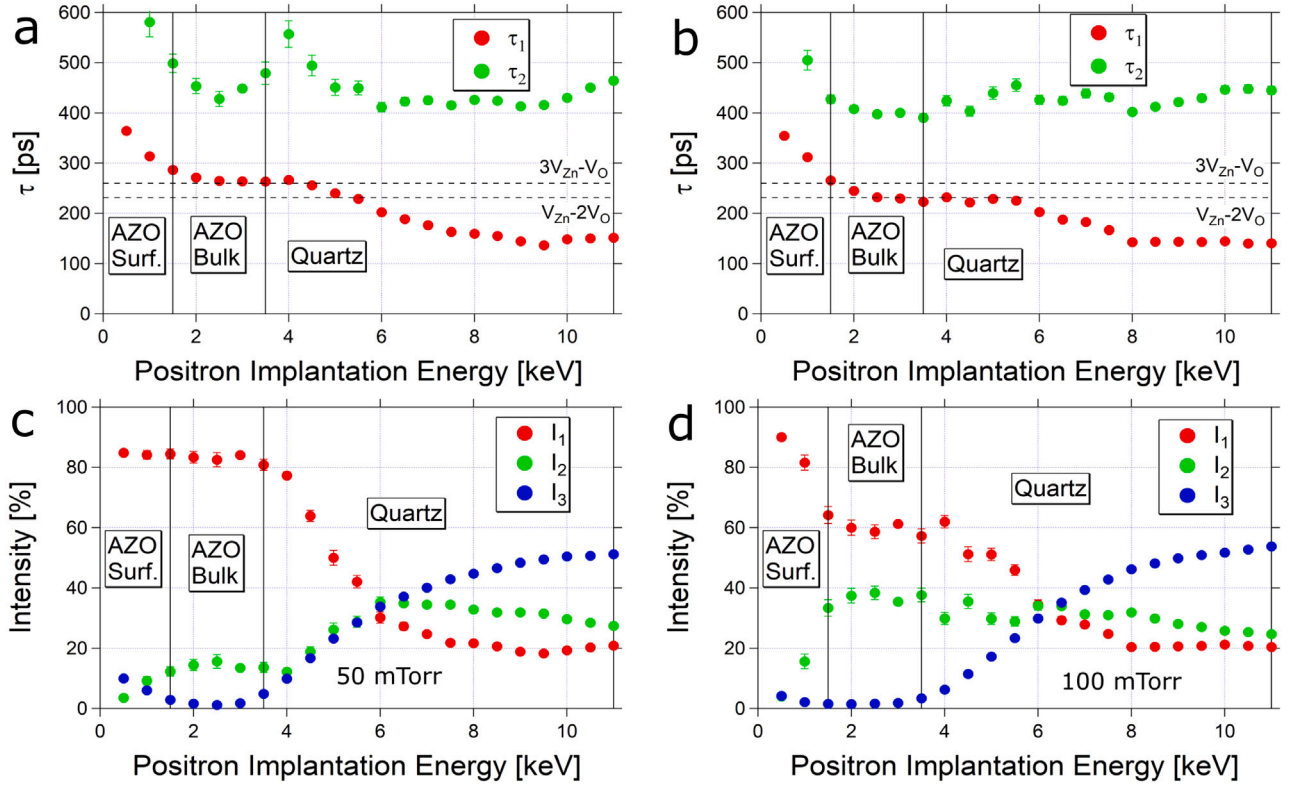

Fig. 6. VEPALS depth profiles for the AZO/Quartz films. **(a)** Lifetimes in the film deposited at 50 mTorr, **(b)** lifetimes in the film deposited at 100 mTorr, **(c)** intensities in the film deposited at 50 mTorr and **(d)** intensities in the film deposited at 100 mTorr. Dotted lines mark the calculated lifetimes associated to the $3V_{Zn} - V_O$ and $V_{Zn} - 2V_O$ vacancy clusters. Regions assigned to the layers are marked. The error bars are within the dots size if not visible.

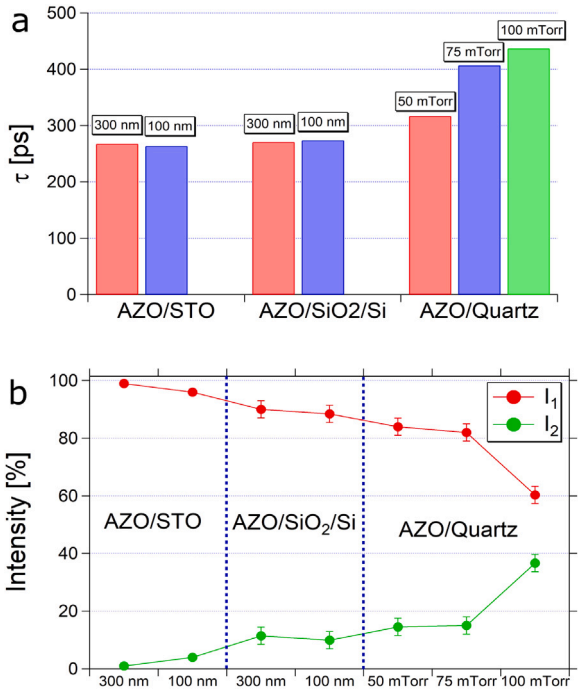

Fig. 7. (a) Average positron lifetime and **(b)** average intensities of the first two components of the lifetime spectra in the AZO films deposited on different substrates.

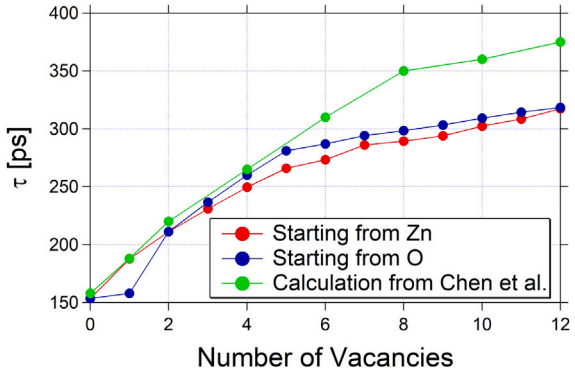

Fig. 8. Calculated positron lifetimes (ATSUP code, BN scheme) for spherical vacancy clusters with increasing size, starting from Zn or O as center atom, plus calculations from Chen et al. [62].

3.4. Doppler Broadening Spectroscopy

DBS depth profiling has been performed in the range 0.5–35 keV for all the samples. The $S(E)$ and $W(E)$ curves were successfully fitted by fixing the known densities (3.58 g/cm^3 for MgO, 5.61 g/cm^3 for ZnO, 5.11 g/cm^3 for STO, 2.2 g/cm^3 for SiO_2 and 2.33 g/cm^3 for Si) and thicknesses of the layers (20 nm for the MgO capping and 650 nm for the thermal SiO_2).

The $S(E)$ and $W(E)$ curves for the AZO/STO and AZO/SiO_2/Si films are shown in Fig. 9. The values have been normalized to the ZnO bulk single crystal reference, shown in Fig. 1 of the SI. The first part of the curves until 1.5–2 keV is identical for all the samples and represents annihilations at the surface and in the MgO capping layer, which is expected to be rather defective. Indeed, it was nicely fitted

Table 3
Positron lifetimes for small vacancy clusters up to four vacancies evaluated with the ATSUP code in this work and other calculation from literature.

Annihilation state	Lifetime [ps]	Method
Bulk	154 (This work)	ATSUP-BN, no relaxation
	159 [30]	ATSUP-BN, no relaxation
	~ 160 [62]	ATSUP-SM, no relaxation
	~ 160 [34]	ATSUP-BN, no relaxation
	161 [63]	ATSUP-BN, no relaxation
V_O	158 (This work)	ATSUP-BN, no relaxation
	159 [30]	ATSUP-BN, with relaxation
	160 [30]	ATSUP-BN, no relaxation
	~ 160 [34]	ATSUP-BN, no relaxation
	169 [63]	ATSUP-BN, no relaxation
V_{Zn}	188 (This work)	ATSUP-BN, no relaxation
	~ 188 [62]	ATSUP-SM, no relaxation
	194 [30]	ATSUP-BN, no relaxation
	~ 195 [34]	ATSUP-BN, no relaxation
	196 [63]	ATSUP-BN, no relaxation
	~ 205 [34]	ATSUP-BN, with relaxation
	229 [30]	ATSUP-BN, with relaxation
$V_{Zn} - V_O$	211 (This work)	ATSUP-BN, no relaxation
	~ 220 [34]	ATSUP-BN, no relaxation
	~ 220 [62]	ATSUP-SM, no relaxation
	223 [63]	ATSUP-BN, no relaxation
	223–224 [30]	ATSUP-BN, no relaxation
	276–286 [30]	ATSUP-BN, with relaxation
$V_{Zn} - 2V_O$	231 (This work)	ATSUP-BN, no relaxation
	~ 240 [34]	ATSUP-BN, no relaxation
$2V_{Zn} - V_O$	237 (This work)	ATSUP-BN, no relaxation
	254 [63]	ATSUP-BN, no relaxation
$2(V_{Zn} - V_O)$	~ 265 [62]	ATSUP-SM, no relaxation
$V_{Zn} - 3V_O$	250 (This work)	ATSUP-BN, no relaxation
	~ 265 [34]	ATSUP-BN, no relaxation
$3V_{Zn} - V_O$	260 (This work)	ATSUP-BN, no relaxation

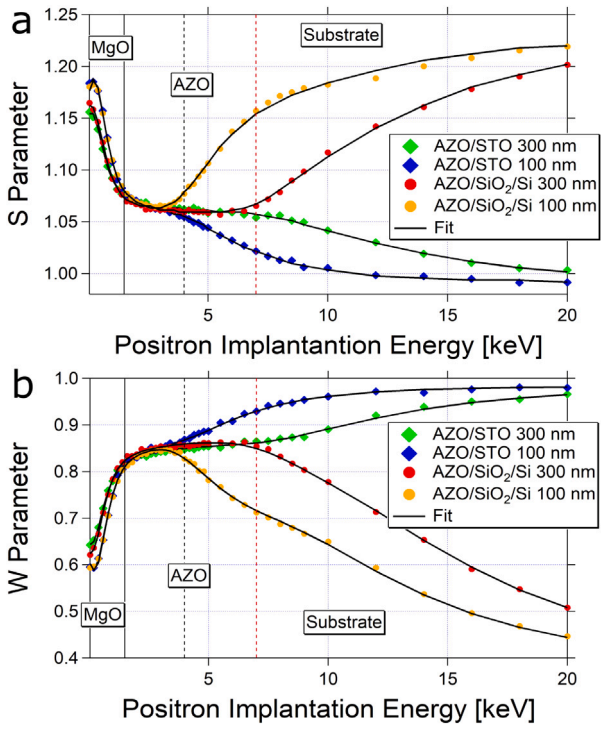

Fig. 9. **(a)** $S(E)$ and **(b)** $W(E)$ curves for the AZO/STO and AZO/SiO_2/Si films and fits with the diffusion-annihilation equation. Dotted lines (black for 100 nm thick films and red for 300 nm thick films) represent the AZO/substrate interface. The error bars are within the dots size if not visible.

with a positron diffusion length L_+ of 4 nm, which is much smaller than its thickness of 20 nm. From the DBS depth profiles we can easily appreciate the different thicknesses of the AZO films, which are comprised in the energy regions 2–4.5 for 100 nm thick films and 2–7.5 for 300 nm thick films. The STO substrate has a lower S parameter and an higher W parameter than the films, which are recognizable as plateaus in the curves. The STO shows also a positron diffusion length around 50 nm and allows back-diffusion of positrons into the film. This fact is reflected in a region of smooth change between the parameters of the film and of the substrate. In any case, it can be seen, looking at the film regions, that the S and W parameters of both the AZO/STO films are similar.

If we look to the $S(E)$ and $W(E)$ curves for the AZO/SiO_2/Si films, instead, we immediately see the different substrate, which has completely different S and W parameters with respect to both the AZO and the STO, while the surface dynamics is similar. This fact helps identifying the energy regions of the films, which are far more manifest as a minimum/maximum in the $S(E)$ and $W(E)$ curves but they are clearly similar to the ones of the AZO/STO films, since the thicknesses are the same. Here there is a much abrupt change between film and substrate, because the diffusion length of the SiO_2 is very short, and it is smaller even in the polycrystalline films with respect to the epitaxial ones. Even in this case, it can be seen that the S and W parameters of the films are quite similar, also with respect to AZO/STO films.

The picture changes in the DBS depth profiles of AZO/Quartz films, shown in Fig. 10. Here the thickness is fixed to 100 nm and there is no capping, and indeed the films are enclosed approximately in the region 1.5–3.5 keV. The S parameter of the films drastically increases (and the W parameter decreases) when the Ar pressure is increased. This means the defectivity of the samples is changing in accordance with VEPALS measurements. Indeed, an increase of the S parameter (and decrease of the W parameter) is associated with more annihilations in defect sites and/or annihilations in larger vacancy complexes, since positrons trapped into open volume defects will annihilate with less core electrons and more valence ones.

The total picture is shown in Table 4, where the normalized S and W parameters and the fitted positron diffusion lengths L_+ of the films, which were used to estimate the defect concentration C_d, are listed. Since from PALS, we know that we are in saturation trapping, the S and W values reflect purely the major defects.

Nevertheless, even if we are in positron trapping saturation regime, we can evaluate the overall defect concentration by comparing the fitted positron diffusion length L_+ with the calculated defect-free one $L_{+,B}$, since it continues to decrease with increasing defect density even in the case of positron trapping saturation, which is not the case with other positron annihilation parameters [48]. The corresponding defect concentration C_d can be estimated via the following relationship [38]

$$C_d = \frac{N}{\mu_V \tau_B}\left(\frac{L_{+,B}^2}{L_+^2} - 1\right) \tag{4}$$

where N is the atomic density ($8.3 \cdot 10^{22}$ cm^{-3} for ZnO), μ_V is the positron specific trapping rate and τ_B is the ZnO bulk lifetime of 154 ps, as calculated. $L_{+,B}$ has been calculated as 280 nm [33]. To calculate the concentration of defects, due to the fact that the specific trapping rate μ_V is not know for small vacancy clusters, we assume as an approximation that the specific trapping rate for the cluster is the specific trapping rate for a neutral vacancy, which is $\sim 1 \cdot 10^{15}$ s^{-1} according to Tuomisto and Makkonen [22], multiplied for the number of vacancies (four except for the AZO/Quartz film grown at 100 mTorr where they are three) in the cluster.

We observe that L_+ is almost the same around 30 nm for the 300 nm thick AZO/STO and AZO/SiO_2/Si films, while it is quite different for the corresponding 100 nm thick films, decreasing from 26 nm in the epitaxial one to 13 nm for the polycrystalline one. This is in line with

Table 4
Summary of the results of the analysis of the DBS depth profiles, with relative S and W parameters, fitted diffusion length and extracted overall defect concentration.

Sample	Relative S parameter	Relative W parameter	L_+ [nm]	C_d [cm^{-3}]
AZO/STO 300 nm	1.058 ± 0.001	0.860 ± 0.003	34.5 ± 4.3	$(8.7 \pm 2.3) \cdot 10^{18}$
AZO/STO 100 nm	1.061 ± 0.002	0.860 ± 0.004	26.0 ± 2.7	$(1.5 \pm 0.3) \cdot 10^{19}$
AZO/SiO_2/Si 300 nm	1.057 ± 0.001	0.868 ± 0.003	30.5 ± 1.7	$(1.1 \pm 0.1) \cdot 10^{19}$
AZO/SiO_2/Si 100 nm	1.058 ± 0.001	0.860 ± 0.003	13.0 ± 2.0	$(6.2 \pm 2.0) \cdot 10^{19}$
AZO/Quartz 50 mTorr	1.080 ± 0.001	0.821 ± 0.003	10.5 ± 2.0	$(9.6 \pm 3.9) \cdot 10^{19}$
AZO/Quartz 75 mTorr	1.132 ± 0.001	0.741 ± 0.003	9.0 ± 2.0	$(1.3 \pm 0.6) \cdot 10^{20}$
AZO/Quartz 100 mTorr	1.148 ± 0.001	0.724 ± 0.003	4.4 ± 1.1	$(5.5 \pm 3.1) \cdot 10^{20}$

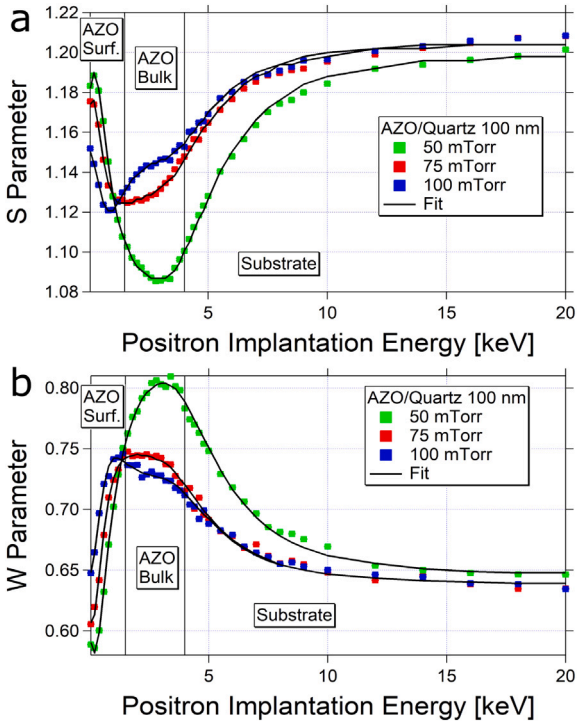

Fig. 10. **(a)** $S(E)$ and **(b)** $W(E)$ curves for the AZO/Quartz films and fits with the diffusion-annihilation equation. The error bars are within the dots size if not visible.

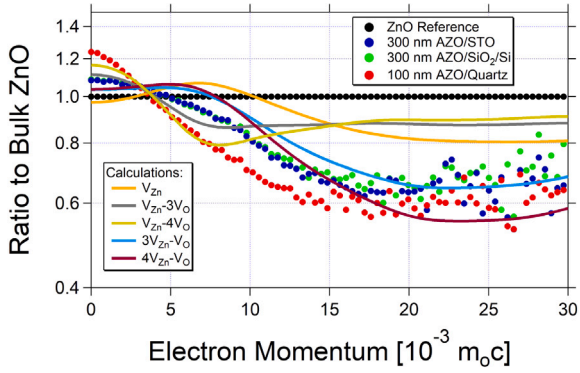

Fig. 11. CDBS ratio curves to ZnO of the selected samples together with ATSUP calculations of some small vacancy clusters included.

the decrease of crystalline quality of polycrystalline films when the thickness is decreased [7]. The L_+ also decreases with pressure in the AZO/Quartz films, from around 10 nm in the sample grown at a pressure of 50 mTorr to around 4 nm for the one grown at 100 mTorr. As reported in Table 4, the epitaxial AZO/STO and polycrystalline AZO/SiO_2/Si films have a defect concentration in the 10^{18}–10^{19} cm^{-3} order of magnitude, while the AZO/Quartz films deposited at the highest Ar pressures reach defect concentrations of the order of 10^{20} cm^{-3}. The increase in defect concentration for these samples is in line with their decreasing crystalline quality.

3.5. Coincidence Doppler Broadening Spectroscopy

For CDBS we selected three samples, the 300 nm thick AZO/STO and AZO/SiO_2/Si films and the 100 nm thick AZO/Quartz film deposited at 100 mTorr, and an implantation energy in order to maximize the positron annihilation into the films, which correspond to 5 keV for the 300 nm thick films and 2 keV for the 100 nm thick one. This is because to get reliable CDBS data, long measurement times are required. To construct ratio curves, we measured our ZnO bulk single crystal and a Zn bulk crystal.

From the CDBS ratio curves to ZnO in Fig. 11 it can be seen that all the AZO samples are quite defected, since the high-momentum amplitude (above $10 \cdot 10^{-3} m_0 c$) is far away from the ZnO reference (low W parameter) and also the low-momentum part is high (high S parameter).

The data of the 300 nm thick AZO/STO and AZO/SiO_2/Si are very similar, while the 100 nm thick AZO/Quartz shows marked differences with respect to them and thus is considerably more defective and shows different type of defects. From comparison with calculated ratio curves for defects, we can individuate what is the main annihilation site for positrons in the sample, keeping in mind that, since the ATSUP codes only considers core electrons, the low momentum part of calculated ratio curves cannot be trusted and only taken as a rough indication. Therefore, the ratio curves are typically only reliable for electron momenta above $10 \cdot 10^{-3} m_0 c$ [74].

In literature there are some calculations for CDBS ratio curves of small vacancy defects in ZnO, with the projector augmented-wave method and considering lattice relaxation [31,35,75]. Anyway, these calculated curves, even if they consider relaxation, do not match well with our experimental data. In fact, our experimental curves in the high momentum region (above $15 \cdot 10^{-3} m_o c$) are all below 0.7 of ratio with bulk ZnO, while the ratio curves in the literature, which are all for small vacancy complexes, always stay above 0.7. An exception are the curves from Chen et al. [35] for the simple V_{Zn} and the $V_{Zn} - V_O$, which however show an oscillating behavior in the high momentum zone which is not observed in our experimental curves. Hence, by looking at the high momentum part of the ratio curves and comparing them with ATSUP calculations in Fig. 11, it can be concluded that the leading defect in the AZO/STO and AZO/SiO_2/Si films is the $3V_{Zn} - V_O$. In fact, the ratio curve for the other calculated four vacancy complex, the $V_{Zn} - 3V_O$, is definitely too high with respect to experimental data in the high-momentum region. In the AZO/Quartz films grown at 100 mTorr, instead, we know the defect balance is different, around 60% of intensity for small and 40% for large complexes. The CDBS ratio curve results from both annihilation channels, hence the large difference of the ratio curve of this sample with respect to the others underlines the different quality of the defects and the increased defectivity in this film.

The CDBS ratio curves to Zn, shown in Fig. 12, are all characterized by a peak in the region $p = 5 \cdot 10^{-3} m_0 c$, which is a fingerprint of annihilation of positrons with electrons of O atoms. This is typical

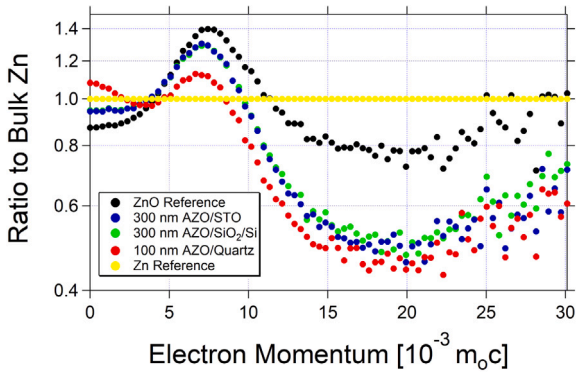

Fig. 12. CDBS ratio curves to Zn of the selected samples.

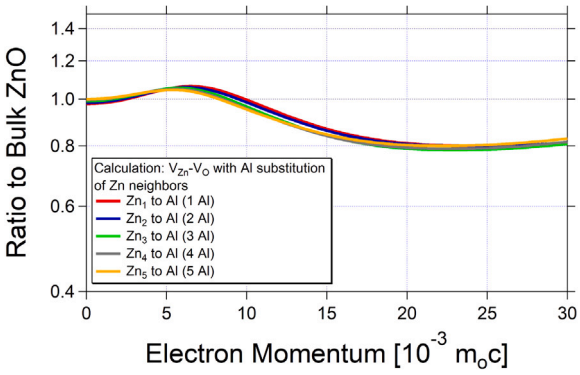

Fig. 13. CDBS calculated ratio curves for a ZnO di-vacancy with increasing number of neighboring Zn atoms substituted with Al.

for cation vacancies in oxides, like V_{Zn} in ZnO, which are clearly surrounded by O atoms. The peak is less pronounced for the 100 nm thick AZO/Quartz. This means that the positrons are seeing less oxygen and this can be linked to the bigger size of the defects.

As anticipated, with CDBS it is possible to evaluate the chemical surroundings of the annihilation environment, hence we exploited it to check whether or not we have defect decoration with Al on Zn sites. To do it we calculated the ratio curves for a ZnO di-vacancy with increasing number of neighboring Zn atoms substituted with Al. From comparison between the calculated curves reported in Fig. 13, the effects of defect decoration with Al are hardly visible in high-momentum ratio curves, even when 5 neighboring Zn atoms are substituted with Al.

By looking in Fig. 14 at the positron lifetimes calculated by sequentially replacing by Al the nearest Zn neighbors of single V_O and V_{Zn}, di-vacancy $V_{Zn} - V_O$ and triple vacancies $V_{Zn} - 2V_O$ and $2V_{Zn} - V_O$, it can be observed that Al decoration tend to slightly reduce the lifetime. Only extremely high Al substitutions would be detectable, much beyond the Al content of these samples, and only for the decoration of the single V_{Zn} and the $V_{Zn} - V_O$ di-vacancy. Therefore, Al decoration of vacancy defects in this system is not expected to be visible.

4. Conclusions

In conclusion, we present a complete study of the point defect dynamics of 4 at.% AZO thin films grown by RF magnetron sputtering on different substrates, STO, SiO_2/Si and UV fused quartz. The films were characterized by different thicknesses and crystalline order, which was varied through the choice of the substrate and the deposition conditions and ranged from epitaxial, to polycrystalline and to partially amorphous. We performed a structural characterization through XRD

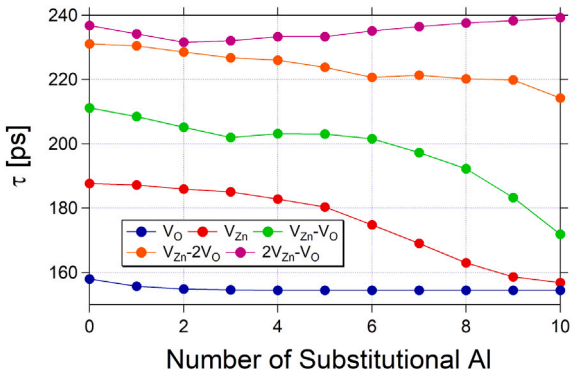

Fig. 14. Calculated positron lifetimes for different vacancy-defects with increasing amount of Al substitution of neighboring Zn atoms.

and TEM, and we proved that AZO/STO films were epitaxial and increasing the Ar pressure in the deposition of AZO/Quartz films up to 100 mTorr drastically decreased the typical preferred c-axis orientation of AZO films and the crystalline quality in general, introducing a good degree of amorphization of around 33% for a film grown at 100 mTorr.

The defectivity of the films have been investigated through depth-resolved Variable Energy PALS, DBS and CDBS techniques. ATSUP calculations were performed in order to unveil the lifetimes and the Doppler broadening associated to defects in the ZnO lattice. We individuated the main defect in the films which is a four vacancy cluster $3V_{Zn} - V_O$ with an intensity of around 95% in AZO/STO films and more than 80% in AZO/SiO_2/Si films. The remaining intensity in the latter was associated to a longer lifetime, which we label to much larger vacancy clusters located in grain boundaries. In AZO/Quartz film grown at high pressure these larger vacancy clusters, located either at grain boundaries or in the amorphous regions of the film, reach almost the 40% of the intensity, and also some very long component appear, which are probably due to some pores and voids already spotted by TEM measurements. Nevertheless, in this film the leading defect is a bit smaller than in other samples, being a three vacancy cluster, the $V_{Zn} - 2V_O$ or the $2V_{Zn} - V_O$ complex. With DBS, we evaluated the positron diffusion length and from it we extracted the overall defect concentration, which ranges from 10^{18}–10^{19} cm^{-3} for epitaxial and polycrystalline films to 10^{20} cm^{-3} for partially amorphous films.

To summarize, thanks to the unique sensitivity of PAS to open volume defects in solids, we offer a total description of the defect dynamics of AZO thin films when their crystalline quality is varied. These results can be important for further development of application of TCO films, since their properties are strongly linked to the presence of point defects.

CRediT authorship contribution statement

R. Magrin Maffei: Writing – review & editing, Writing – original draft, Project administration, Methodology, Investigation, Formal analysis, Data curation, Conceptualization. **M. Butterling:** Writing – review & editing, Software, Methodology, Investigation, Data curation. **M.O. Liedke:** Writing – review & editing, Methodology, Data curation. **S. D'Addato:** Writing – review & editing, Supervision. **A. di Bona:** Writing – review & editing, Supervision. **G. Bertoni:** Writing – review & editing, Investigation, Funding acquisition, Formal analysis, Data curation. **G.C. Gazzadi:** Writing – review & editing, Investigation, Data curation. **S. Mariazzi:** Writing – review & editing, Methodology. **A. Wagner:** Writing – review & editing, Resources, Methodology. **R.S. Brusa:** Writing – review & editing, Supervision, Resources, Methodology, Data curation, Conceptualization. **S. Benedetti:** Writing – review & editing, Supervision, Resources, Funding acquisition, Data curation.

Declaration of competing interest

The authors declare that they have no known competing financial interests or personal relationships that could have appeared to influence the work reported in this paper.

Data availability

Data will be made available on request.

Acknowledgments

The authors thank the financial support from Next Generation EU through the MUR PRIN 2022 AMONIX 2022BTMXZT and the PNRR Infrastructure for Energy Transition and Circular Economy - iENTRANCE@ENL IR0000027. Parts of this research were carried out at ELBE at the Helmholtz-Zentrum Dresden-Rossendorf e.V., a member of the Helmholtz Association. We would like to thank the facility staff (Eric Hirschmann and Ahmed G. Attallah) for assistance.

Appendix A. Supplementary data

Supplementary material related to this article can be found online at https://doi.org/10.1016/j.apsusc.2024.160240.

References

[1] K. Ellmer, A. Klein, B. Rech, Transparent Conductive Zinc Oxide, Vol. 104, Springer Series in Material Science, 2008.
[2] K. Ellmer, Past achievements and future challenges in the development of optically transparent electrodes, Nature Photon. 6 (2012) 809–817.
[3] G.V. Naik, V.M. Shalaev, A. Boltasseva, Alternative plasmonic materials: beyond gold and silver, Nature Photon. 25 (24) (2013) 3264–3294.
[4] R.A. Afre, N. Sharma, M. Sharon, M. Sharon, Transparent conducting oxide films for various applications: a review, Rev. Adv. Mater. Sci. 53 (1) (2018) 79–89.
[5] Y. Chen, Review of ZnO transparent conducting oxides for solar applications, IOP Conf. Ser.: Mater. Sci. Eng. 423 (2018) 012170.
[6] H. Dondapati, K. Santiago, A.K. Pradhan, Influence of growth temperature on electrical, optical, and plasmonic properties of aluminum:zinc oxide films grown by radio frequency magnetron sputtering, J. Appl. Phys. 114 (14) (2013) 143506.
[7] R.M. Maffei, A. di Bona, M. Sygletou, F. Bisio, S. D'Addato, S. Benedetti, Suppression of grain boundary contributions on carrier mobility in thin Al-doped ZnO epitaxial film, Appl. Surf. Sci. 624 (2023) 157133.
[8] M.D. McCluskey, S.J. Jokela, Defects in ZnO, J. Appl. Phys. 106 (7) (2009) 071101.
[9] A. Janotti, C.G.V. de Walle, Fundamentals of zinc oxide as a semiconductor, Rep. Progr. Phys. 72 (12) (2009) 126501.
[10] I. Ayoub, V. Kumar, R. Abolhassani, R. Sehgal, V. Sharma, R. Sehgal, H.C. Swart, Y.K. Mishra, Advances in ZnO: Manipulation of defects for enhancing their technological potentials, Nanotechnol. Rev. 11 (1) (2022) 575–619.
[11] S. Lany, A. Zunger, Dopability, intrinsic conductivity, and nonstoichiometry of transparent conducting oxides, Phys. Rev. Lett. 98 (4) (2007) 045501.
[12] E. Menendez-Proupin, P. Palacios, P. Wahnon, Electronic and atomic structure of complex defects in Al- and Ga-highly doped ZnO films, Mater. Chem. Phys. 160 (2015) 420–428.
[13] A. Catellani, A. Ruini, A. Calzolari, Optoelectronic properties and color chemistry of native point defects in Al:ZnO transparent conductive oxide, J. Mater. Chem. C 3 (32) (2015).
[14] A.F. Kohan, G. Ceder, D. Morgan, C.G.V. de Walle, First-principles study of native point defects in ZnO, Phys. Rev. B 61 (22) (2000) 15019.
[15] A. Janotti, C.G.V. de Walle, Native point defects in ZnO, Phys. Rev. B 76 (16) (2007) 165202.
[16] F. Tuomisto, V. Ranki, K. Saarinen, D.C. Look, Evidence of the Zn vacancy acting as the dominant acceptor in n-type ZnO, Phys. Rev. Lett. 91 (20) (2003) 1–4.
[17] F. Tuomisto, K. Saarinen, D.C. Look, G.C. Farlow, Introduction and recovery of point defects in electron-irradiated ZnO, Phys. Rev. B 72 (8) (2005) 085206.
[18] F. Tuomisto, Open volume defects: positron annihilation spectroscopy, in: B.G. Svensson, S.J. Pearton, C. Jagadish (Eds.), Semiconductors and Semimetals, Vol. 88, Elsevier, Amsterdam, The Netherlands, 2013.
[19] P.J. Schultz, K.G. Lynn, Interaction of positron beams with surfaces, thin films, and interfaces, Rev. Mod. Phys. 60 (3) (1988) 701.
[20] P. AsokaKumar, K.G. Lynn, D.O. Welch, Characterization of defects in Si and SiO_2-Si using positrons, J. Appl. Phys. 76 (9) (1994) 4935.
[21] R. Krause-Rehberg, H.S. Leipner, Positron annihilation, in: Semiconductors: Defect Studies, Vol. 127, Springer Science & Business Media, Luxemburg, 1999.
[22] F. Tuomisto, I. Makkonen, Defect identification in semiconductors with positron annihilation: experiment and theory, Rev. Mod. Phys. 85 (4) (2013) 1583.
[23] R.S. Brusa, A. Dupasquier, Positronium emission and cooling, in: Proceedings of the International School of Physics "Enrico Fermi", IOS Press, Amsterdam, 2009.
[24] M. Alatalo, H. Kauppinen, K. Saarinen, M.J. Puska, J. Mäkinen, P. Hautojärvi, R.M. Nieminen, Identification of vacancy defects in compound semiconductors by core-electron annihilation: Application to InP, Phys. Rev. B 51 (7) (1995) 4176.
[25] M. Alatalo, B. Barbiellini, M. Hakala, H. Kauppinen, T. Korhonen, M.J. Puska, K. Saarinen, P. Hautojärvi, R.M. Nieminen, Theoretical and experimental study of positron annihilation with core electrons in solids, Phys. Rev. B 54 (4) (1996) 2397.
[26] P. Asoka-Kumar, M. Alatalo, V.J. Ghosh, A.C. Kruseman, B. Nielsen, K.G. Lynn, Increased elemental specificity of positron annihilation spectra, Phys. Rev. Lett. 77 (10) (1996) 2097.
[27] C. Macchi, A. Somoza, J. Guimpel, S. Suarez, W. Egger, C. Hugenschmidt, S. Mariazzi, R.S. Brusa, Oxygen related defects and vacancy clusters identified in sputtering grown UO_x thin films by positron annihilation techniques, Results Phys. 27 (2021) 104513.
[28] A. Dupasquier, G. Kogel, A. Somoza, Studies of light alloys by positron annihilation techniques, Acta Mater. 52 (16) (2004) 4707–4726.
[29] R.S. Brusa, W. Deng, G.P. Karwasz, A. Zecca, Doppler-broadening measurements of positron annihilation with high-momentum electrons in pure elements, Nucl. Instrum. Methods Phys. Res. B 194 (4) (2002) 519–531.
[30] G. Brauer, W. Anwand, W. Skorupa, J. Kuriplach, O. Melikhova, C. Moisson, H. von Wenckstern, H. Schmidt, M. Lorenz, M. Grundmann, Defects in virgin and N^+-implanted ZnO single crystals studied by positron annihilation, hall effect, and deep-level transient spectroscopy, Phys. Rev. B 74 (4) (2006) 045208.
[31] Z.Q. Chen, K. Betsuyaku, A. Kawasuso, Vacancy defects in electron-irradiated ZnO studied by Doppler broadening of annihilation radiation, Phys. Rev. B 77 (11) (2008) 113204.
[32] G. Brauer, W. Anwand, D. Grambole, J. Grenzer, W. Skorupa, J. Čížek, J. Kuriplach, I. Procházka, C.C. Ling, C.K. So, D. Schulz, D. Klimm, Identification of Zn-vacancy–hydrogen complexes in ZnO single crystals: A challenge to positron annihilation spectroscopy, Phys. Rev. B 79 (11) (2009) 115212.
[33] F. Lukác, J. Čížek, I. Procházka, O. Melikhova, W. Anwand, G. Brauer, Defects studies of ZnO single crystals prepared by various techniques, Acta Phys. Pol. A 125 (3) (2014).
[34] I. Procházka, J. Čížek, F. Lukác, O. Melikhova, J. Valenta, V. Havranek, W. Anwand, V.A. Skuratov, T.S. Strukova, Characterisation of irradiation-induced defects in ZnO single crystals, J. Phys.: Conf. Ser. 674 (2016) 012014.
[35] A. Zubiaga, F. Tuomisto, V.A. Coleman, H.H. Tan, C. Jagadish, K. Koike, S. Sasa, M. Inoue, M. Yano, Mechanisms of electrical isolation in O^+-irradiated ZnO, Phys. Rev. B 78 (3) (2008) 035125.
[36] F. Tuomisto, C. Rauch, M.R. Wagner, A. Hoffmann, S. Eisermann, B.K. Meyer, L. Kilanski, M.C. Tarun, M.D. McCluskey, Nitrogen and vacancy clusters in ZnO, J. Mater. Res. 28 (15) (2013).
[37] S. Särkijärvi, S. Sintonen, F. Tuomisto, M. Bosund, S. Suihkonen, H. Lipsanen, Effect of growth temperature on the epitaxial growth of ZnO on GaN by ALD, J. Cryst. Growth 398 (2014) 18–22.
[38] Z. Wang, C. Luo, W. Anwand, A. Wagner, M. Butterling, M.A. Rahman, M.R. Phillips, C. Ton-That, M. Younas, S. Su, F.C.-C. Ling, Vacancy cluster in ZnO films grown by pulsed laser deposition, Sci. Rep. 9 (2019) 3534.
[39] S. Prucnal, J. Wu, Y. Berencén, M.O. Liedke, A. Wagner, F. Liu, M. Wang, L. Rebohle, S. Zhou, H. Cai, W. Skorupa, Engineering of optical and electrical properties of ZnO by non-equilibrium thermal processing: The role of zinc interstitials and zinc vacancies, J. Appl. Phys. 122 (3) (2017) 035303.
[40] D. Scorticati, A. Illiberi, T.C. Bor, S.W.H. Eijt, H. Schut, G.R.B.E. Römer, M.K. Gunnewiek, A.T.M. Lenferink, B.J. Kniknie, R.M. Joy, M.S. Dorenkamper, D.F. de Lange, C. Otto, D. Borsa, W.J. Soppe, A.J.H. in 't Veld, Thermal annealing using ultra-short laser pulses to improve the electrical properties of Al:ZnO thin films, Acta Mater. 98 (2015) 327–335.
[41] W. Shi, M. Theelen, A. Illiberi, N. Barreau, S.J. van der Sar, M. Butterling, H. Schut, W. Egger, M. Dickmann, C. Hugenschmidt, M. Zeman, E. Brück, S.W.H. Eijt, Evolution and role of vacancy clusters at grain boundaries of ZnO:Al during accelerated degradation of Cu(In, Ga)Se_2 solar cells revealed by positron annihilation, Phys. Rev. Mat. 2 (10) (2018) 105403.
[42] I. Valenti, S. Benedetti, A. di Bona, V. Lollobrigida, A. Perucchi, P. Di Pietro, S. Lupi, S. Valeri, P. Torelli, Electrical, optical, and electronic properties of Al:ZnO films in a wide doping range, J. Appl. Phys. 118 (16) (2015) 165304.
[43] H. Chou, M.S. Yang, C.P. Wu, Y.C. Tsao, B.J. Chen, T.F. Liao, S.J. Sun, J.W. Chiou, Extended wide band gap amorphous aluminium-doped zinc oxide thin films grown at liquid nitrogen temperature, J. Phys. D: Appl. Phys. 44 (20) (2011) 205404.
[44] T. Minami, T. Miyata, Y. Ohtani, T. Kuboi, Effect of thickness on the stability of transparent conducting impurity-doped ZnO thin films in a high humidity environment, Phys. Status Solidi (RRL) 1 (1) (2007) R31–R33.
[45] T. Minami, T. Kuboi, T. Miyata, Y. Ohtani, Effect of thickness on the stability of transparent conducting impurity-doped ZnO thin films in a high humidity environment, Phys. Status Solidi A 205 (2) (2008) 255–260.

[46] A. Wagner, M. Butterling, M.O. Liedke, K. Potzger, R. Krause-Rehberg, Positron annihilation lifetime and Doppler broadening spectroscopy at the ELBE facility, AIP Conf. Proc. 1970 (1) (2018) 040003.
[47] S. Valkealahti, R.M. Nieminen, MonteCarlo calculations of keV electron and positron slowing down in solids, Appl. Phys. A 35 (1984) 51–59.
[48] F.A. Selim, Positron annihilation spectroscopy of defects in nuclear and irradiated materials - a review, Mater. Charact. 174 (2021) 110952.
[49] E. Hirschmann, M. Butterling, U.H. Acosta, M.O. Liedke, A.G. Attallah, P. Petring, M. Görler, R. Krause-Rehberg, A. Wagner, A new system for real-time data acquisition and pulse parameterization for digital positron annihilation lifetime spectrometers with high repetition rates, J. Instrum. 16 (08) (2021) P08001.
[50] J.V. Olsen, P. Kirkegaard, N.J. Pedersen, M. Eldrup, PALSfit: a new program for the evaluation of positron lifetime spectra, Phys. Status Solidi C 4 (10) (2007) 4004–4006.
[51] W. Anwand, G. Brauer, M. Butterling, H.R. Kissener, A. Wagner, Design and construction of a slow positron beam for solid and surface investigations, Defect Diffus. Forum 331 (2012) 25–40.
[52] C. Hugenschmidt, B. Lowe, J. Mayer, C. Piochacz, P. Pikart, R. Repper, M. Stadlbauer, K. Schreckenbach, Unprecedented intensity of a low-energy positron beam, Nucl. Instrum. Methods A 593 (3) (2008) 616–618.
[53] R.S. Brusa, M.D. Naia, A. Zecca, C. Nobili, G. Ottaviani, R. Tonini, A. Dupasquier, Vacancy-hydrogen interaction in H-implanted si studied by positron annihilation, Phys. Rev. B 49 (11) (1994) 7271.
[54] R.S. Brusa, G.P. Karwasz, N. Tiengo, A. Zecca, F. Corni, R. Tonini, G. Ottaviani, Formation of vacancy clusters and cavities in he-implanted silicon studied by slow-positron annihilation spectroscopy, Phys. Rev. B 61 (15) (2000) 10154.
[55] A. van Veen, H. Schut, M. Clement, J.M.M. de Nijs, A. Kruseman, M.R. Ijpma, VEPFIT applied to depth profiling problems, Appl. Surf. Sci. 85 (1995) 216–224.
[56] M.J. Puska, R.M. Nieminen, Defect spectroscopy with positrons: a general calculational method, J. Phys. F: Met. Phys. 13 (333) (1983).
[57] A.P. Seitsonen, M.J. Puska, R.M. Nieminen, Real-space electronic-structure calculations: Combination of the finite-difference and conjugate-gradient methods, Phys. Rev. B 51 (20) (1995) 14057.
[58] B. Barbiellini, M.J. Puska, T. Korhonen, A. Harju, T. Torsti, R.M. Nieminen, Calculation of positron states and annihilation in solids: A density-gradient-correction scheme, Phys. Rev. B 53 (24) (1996) 16201.
[59] J.M.C. Robles, E. Ogando, F. Plazaola, Positron lifetime calculation for the elements of the periodic table, J. Phys.: Condens. Matter. 19 (17) (2007) 176222.
[60] A.D. Rice, M.O. Liedke, M. Butterling, E. Hirschmann, A. Wagner, N.M. Haegel, K. Alberi, Vacancy complexes in Cd_3As_2, APL Mater. 11 (6) (2023) 061109.
[61] G. Brauer, J. Kuriplach, J. Čížek, W. Anwand, O. Melikhova, I. Prochazka, W. Skorupa, Positron lifetimes in ZnO single crystals, Vacuum 81 (10) (2007) 1314–1317.
[62] Z.Q. Chen, M. Maekawa, S. Yamamoto, A. Kawasuso, X.L. Yuan, T. Sekiguchi, R. Suzuki, T. Ohdaira, Evolution of voids in Al^+-implanted ZnO probed by a slow positron beam, Phys. Rev. B 69 (3) (2004) 035210.
[63] S.K. Sharma, P.K. Pujari, K. Sudarshan, D. Dutta, M. Mahapatra, S.V. Godbole, O.D. Jayakumar, A.K. Tyagi, Positron annihilation studies in ZnO nanoparticles, Solid State Commun. 149 (13–14) (2009) 550–554.
[64] K. Matsubara, P. Fons, A. Yamada, M. Watanabe, S. Niki, Epitaxial growth of ZnO thin films on $LiNbO_3$ substrates, Thin Solid Films 347 (1–2) (1999) 238–240.
[65] H.F. McMurdie, M.C. Morris, E.H. Evans, B. Paretzkin, W. Wong-Ng, L. Ettlinger, C.R. Hubbard, Powder Diffr. 1 (76) (1986).
[66] M. Mizuno, H. Araki, Y. Shirai, Theoretical calculations of positron lifetimes for metal oxides, Mater. Trans. 45 (7) (2004) 1964–1967.
[67] S. Dutta, M. Chakrabarti, S. Chattopadhyay, D. Jana, D. Sanyal, A. Sarkar, Defect dynamics in annealed ZnO by positron annihilation spectroscopy, J. Appl. Phys. 98 (5) (2005) 053513.
[68] M.J. Puska, S. Makinen, M. Manninen, R.M. Nieminen, Screening of positrons in semiconductors and insulators, Phys. Rev. B 39 (11) (1989) 7666.
[69] R.C. Hoffmann, S. Sanctis, M.O. Liedke, M. Butterling, A. Wagner, C. Njel, J.J. Schneider, Zinc oxide defect microstructure and surface chemistry derived from oxidation of metallic zinc: Thin-film transistor and sensor behavior of ZnO films and rods, Chem. A Eur. J. 27 (17) (2021) 5422–5431.
[70] H.S. Domingos, J.M. Carlsson, P.D. Bristowe, B. Hellsing, The formation of defect complexes in a ZnO grain boundary, Interface Sci. 12 (2004) 227–234.
[71] R. Ono, T. Togimitsu, W. Sato, Evaluation of vacancy-type defects in ZnO by the positron annihilation lifetime spectroscopy, J. Radioanal. Nucl. Chem. 303 (2015) 1223–1226.
[72] A. Karbowski, K. Fedus, J. Patyk, L. Bujak, K. Sluzewski, G. Karwasz, Photoluminescence and positron annihilation lifetime studies on pellets of ZnO nanocrystals, Nukleonika 58 (1) (2013) 189–194.
[73] D. Wang, Z.Q. Chen, D.D. Wang, N. Qi, J. Gong, C.Y. Cao, Z. Tang, Positron annihilation study of the interfacial defects in ZnO nanocrystals: Correlation with ferromagnetism, J. Appl. Phys. 107 (2) (2010) 023524.
[74] J. Čížek, Characterization of lattice defects in metallic materials by positron annihilation spectroscopy: A review, J. Mater. Sci. Technol. 34 (4) (2018) 577.
[75] I. Makkonen, E. Korhonen, V. Prozheeva, F. Tuomisto, Identification of vacancy defect complexes in transparent semiconducting oxides ZnO, In_2O_3 and SnO_2, J. Phys.: Condens. Matter. 28 (22) (2016) 224002.